Ahmad Sohankar
Assistant Professor

L. Davidson
Professor

Thermo and Fluid Dynamics,
Chalmers University of Technology,
SE-412 96 Göteborg, Sweden

C. Norberg
Associate Professor
Heat and Power Engineering,
Lund Institute of Technology, Box 118,
SE-221 00 Lund, Sweden

Large Eddy Simulation of Flow Past a Square Cylinder: Comparison of Different Subgrid Scale Models

Large eddy simulation of flow past a rigid prism of a square cross section with one side facing the oncoming flow at $Re = 2.2 \times 10^4$ is performed. An incompressible code is used employing an implicit fractional step method finite volume with second-order accuracy in space and time. Three different subgrid scale models: the Smagorinsky, the standard dynamic, and a dynamic one-equation model, are applied. The influence of finer grid, shorter time step, and larger computational spanwise dimension is investigated. Some global quantities, such as the Strouhal number and the mean and rms values of lift and drag, are computed. A scheme for correcting the global results for blockage effects is presented. By comparison with experiments, the results produced by the dynamic one-equation one give better agreement with experiments than the other two subgrid models.
[S0098-2202(00)01001-4]

1 Introduction

The flow around bluff bodies, such as cylinders and prisms, is of relevance to technical problems associated with energy conversion and structural design and arises in many industrial applications and environmental situations. In recent years, researchers' attention has turned to the use of large eddy simulation (LES) for studying turbulent flow around bluff bodies [1–4]. A LES workshop was held in June 1995 in Germany, and the results are published in Rodi et al. [4]. One of the selected test cases at this workshop is the flow around a square cylinder at zero incidence (one side face facing the oncoming flow) for which LDV measurements are reported [5]. The same flow was considered as test case LES2 at the Second ERCOFTAC Workshop on Direct and Large Eddy Simulation in March 1994. Seven groups took part in the LES2 exercise, and the results of this exercise are reported by Voke [6]. The reason for this focus on LES for the study of flow around bluff bodies has to do with poor results when using statistical turbulence models. Most probably this has to do with complicating factors such as a strongly retarded stagnation flow, massive flow separation, streamline curvature, transition from laminar to turbulent flow, recirculation, vortex shedding, and perhaps most important, the existence of inherent three-dimensional flow structures [7,8]. The presence of sharp corners may also be a complicating factor in flow simulations, especially at high Reynolds numbers.

The main objective of the present study was the examination of different subgrid scale (SGS) models of LES of flow around a square cylinder at $Re = 2.2 \times 10^4$. Another objective was to make a critical evaluation of this selected flow case, in particular on the effects of solid blockage (wall confinement).

2 Configuration and Numerical Details

The flow is described in a Cartesian coordinate system (x, y, z) in which the x axis is aligned with the inlet flow direction, the z axis is parallel with the cylinder axis, and the y axis is perpendicular to both x and z, as shown in Fig. 1. A fixed two-dimensional square cylinder with a side d is exposed to a constant free stream velocity

U_∞. An incompressible flow with constant fluid properties is assumed. The Reynolds number is defined as $Re = U_\infty d/\nu$. All geometrical lengths are scaled with d. Scaling with d also applies for the Strouhal number, $St = f_S d/U_\infty$, where f_S is the shedding frequency for all forces. In the y direction, the vertical distance between the upper and lower walls H defines the solid blockage of the confined flow (blockage parameter $\beta = 1/H$). Velocities are also scaled with U_∞, and physical times with d/U_∞.

Six simulations were performed with different subgrid-scale models: the Smagorinsky model ($C_S = 0.1$), the standard dynamic model, and a new dynamic one-equation model. The influence of finer spatial and temporal resolutions, and the size of the spanwise dimension on the results for the dynamic one-equation subgrid scale model, were also investigated. Details on these simulations are provided in Table 1.

An incompressible finite volume code, based on a fractional step technique and employing a nonstaggered grid arrangement, was used. The scheme is implicit in time, and a second-order Crank–Nicolson scheme was used. All terms were discretized using the second-order central differencing scheme, see [9] for greater detail. The time-marching calculations were started with the fluid at rest, and a constant time step Δt was used. The grid distribution was uniform with a constant cell size Δ_u outside a region from the body, which extended two units upstream, downstream, and sideways (in the x and y directions). The distance from the cylinder surface to the nearest grid point defines δ. For all calculations in this study, $\delta \approx 0.008$. The hyperbolic tangent function was used for stretching the cell sizes between these limits (δ and Δ_u). A uniform grid with a distance of Δ_z between nodes was used in the spanwise direction (z direction, with spanwise
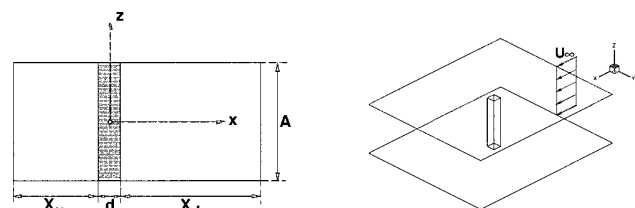

Fig. 1 Flow configuration

Table 1 Summary of computational parameters: (Δt) time step; (Δ_d) uniform cell size downstream of the cylinder downstream the region of a stretching grid; (Δ_u) uniform cell size at upstream and sideways of the cylinder outside the region of stretching grid; (Δ_z) spanwise cell size; (A) computational spanwise dimension

Case	SGS	Grid	Δt	Δ_u	Δ_d	Δ_z	A
SSM	Smagorinsky	185×105×25	0.025	0.25	0.16	0.167	4
DSM	Dynamic	185×105×25	0.025	0.25	0.16	0.167	4
OEDSM	One-equation	185×105×25	0.025	0.25	0.16	0.167	4
OEDSMT	One-equation	185×105×25	0.0125	0.25	0.16	0.167	4
OEDSMF	One-equation	265×161×25	0.025	0.16	0.10	0.167	4
OEDSMA	One-equation	185×105×49	0.025	0.25	0.16	0.146	7

dimension A). The number of nodes distributed over one the cylinder surface was set equal to 25 for all sides of the body and for all simulations except for the case OEDSMF, in which 33 nodes were used (see Table 1).

A uniform flow ($u=1$, $v=w=0$) was prescribed at the inlet, which is located X_u units upstream of the cylinder. At the outlet, located X_d units downstream of the body, the convective boundary condition

$$\frac{\partial u_i}{\partial t} + U_c \frac{\partial u_i}{\partial x} = 0$$

was used for all velocity components. The value of U_c was set equal to U_∞. No-slip conditions were prescribed at the body surfaces. Symmetry conditions simulating a frictionless wall

$$\frac{\partial u}{\partial y} = \frac{\partial w}{\partial y} = v = 0$$

were used at the upper and lower boundaries. A periodic boundary condition was used in the spanwise direction. The normal derivative for the pressure was set to zero at all boundaries. The dimensions X_u, X_d, and H were set to 7.4, 15.8, and 15.7, respectively (see Fig. 1). Computational parameters are listed in Table 1.

3 Subgrid Scale Models

When using LES in the context of the volume average approach (box filter), the time-dependent, three-dimensional Navier–Stokes equations are solved numerically. In this method, the largest scales are resolved numerically, while the unresolved scales must be modeled with a SGS model. The success of LES depends on how accurately the SGS stresses are modeled. The most widely used SGS model is the Smagorinsky model [10]. In this model, the proportionality factor C_S in the SGS stresses is a constant value that must be specified prior to a simulation. The Smagorinsky constant C_S is usually given values between 0.1 and 0.2. In the present study, C_S was set to 0.1. The weak point in this model is that it is not suitable to use a constant that is not really a single universal constant. This model is incapable of taking into account the reduction of length scales near solid walls and thus a damping function is employed in the present study [11]. Also, this model is absolutely dissipative and cannot account for backscatter.

Dynamic models, which are capable of removing some of the drawbacks of the Smagorinsky model, are a suitable alternative. The first attempt to introduce a dynamic SGS eddy viscosity model was developed by Germano et al. [12] and modified by Lilly [13]. One of the drawbacks of the dynamic model is the numerical instability associated with the negative values and large variation of the C coefficient. In the present study, to avoid numerical instability owing to an extensive variation of C in time and space, spatial averaging in the homogeneous z direction and additional local averaging are performed on C. Furthermore, the total viscosity is not allowed to become negative, i.e., $\nu + \nu_t \geq 0$.

3.1 The Dynamic One-Equation Model (OEDSM). Ghosal et al. [14] proposed a dynamic subgrid model without an assumption of any homogeneous flow direction. They tried to optimize the equation for C globally, but still with the constraint that $C > 0$. This optimization leads to an integral equation for obtaining C, whose solution is very expensive and results in an increase in CPU time [14]. In the present study, a new one-equation dynamic subgrid model [15] is used. In this model, the modeled k_{sgs} equation can be written:

$$\frac{\partial k_{sgs}}{\partial t} + \frac{\partial}{\partial x_j}(\bar{u}_j k_{sgs}) = \frac{\partial}{\partial x_j}\left(C_{hom}^k \Delta k_{sgs}^{1/2} \frac{\partial k_{sgs}}{\partial x_j}\right) + P_{k_{sgs}} - C_*^k \frac{k_{sgs}^{3/2}}{\Delta} \tag{1}$$

$$P_{k_{sgs}} = -\tau_{ij}^a \bar{u}_{i,j}, \quad \tau_{ij}^a = -2C^k \Delta k_{sgs}^{1/2} \bar{S}_{ij} = -2\nu_{sgs} \bar{S}_{ij},$$

$$\bar{S}_{ij} = \frac{1}{2}\left(\frac{\partial \bar{u}_i}{\partial x_j} + \frac{\partial \bar{u}_j}{\partial x_i}\right). \tag{2}$$

In the production term, the dynamic coefficient C^k is computed in a way similar to that used in the standard dynamic model [12,16], i.e.,

$$C^k = \frac{\mathcal{L}_{ij} M_{ij}}{2 M_{ij} M_{ij}}, \quad \mathcal{L}_{ij} = \widehat{\overline{u_i u_j}} - \widehat{\overline{u}_i \overline{u}_j}$$

$$K = \widehat{k_{sgs}} + \frac{1}{2}\mathcal{L}_{ii}, \quad M_{ij} = -\widehat{\Delta} K^{1/2} \widehat{\bar{S}}_{ij} + \Delta \widehat{k_{sgs}^{1/2} \bar{S}_{ij}}, \tag{3}$$

where $\mathcal{L}_{ij}$ denotes the *dynamic* Leonard stresses and where $K \equiv \frac{1}{2} T_{ii}$ is the subgrid kinetic energy on the test level [14]. The grid filter width is computed from the cell size, i.e., $\Delta = (\delta V)^{1/3}$, and the test filter is twice as large, i.e., $\widehat{\Delta} = 2\Delta$.

The subgrid turbulent kinetic energy k_{sgs} is essentially a local quantity. Indeed, the Smagorinsky model is based on the assumption of local equilibrium of k_{sgs}, i.e., $P_{k_{sgs}} - \epsilon_{k_{sgs}} = 0$. A slightly better assumption for estimating C_*^k in the dissipation term would be to assume that the filtered right-hand side of the k_{sgs} equation is equal to that of the K equation, i.e.,

$$P_{k_{sgs}} - \frac{1}{\Delta} C_*^k k_{sgs}^{3/2} = P_K - \frac{1}{\widehat{\Delta}} C_*^k K^{3/2} \Rightarrow (C_*^k)^{n+1}$$

$$= \left(P_K - P_{k_{sgs}} + \frac{1}{\Delta}(C_*^k)^n k_{sgs}^{3/2}\right)\frac{\Delta}{K^{3/2}}. \tag{4}$$

Note that $(C_*^k)^n$ has been kept inside the filtering process. The dissipation cannot be negative, which requires that we limit C_*^k to positive values, i.e., $C_*^k \geq 0$.

To ensure numerical stability, a *homogeneous* value of C^k in space (C_{hom}^k) is used in the momentum equations. This is determined by requiring that the production of k_{sgs} in the whole computational domain remains the same, i.e.,

$$\langle 2C^k \Delta k_{sgs}^{1/2} \bar{S}_{ij} \bar{S}_{ij}\rangle_{xyz} = 2C_{hom}^k \langle \Delta k_{sgs}^{1/2} \bar{S}_{ij} \bar{S}_{ij}\rangle_{xyz}. \tag{5}$$

The idea is to include all local dynamic information through the source terms of the transport equation for k_{sgs}. This is probably physically more sound since large local variations in the dynamic

coefficients appear only in the source term, and the effect of the large fluctuations in the dynamic coefficients will be smoothed out in a natural way. In this way, it turns out that the need to average or limit the dynamic coefficients C^k in Eq. (3) and $(C^k_*)^{n+1}$ in Eq. (4) is eliminated altogether.

4 Blockage Corrections

Perhaps the most common scheme for correction of blockage effects in confined incompressible high-Reynolds-number flow around slender bluff bodies is due to Maskell [17]. From experience, see e.g., Maskell, Modi and El-Sherbiny [17,18], the upper limit for confident use of the scheme is about $\beta = 10$ percent. The scheme requires as input the measured/simulated drag coefficient C_D, the measured/simulated base suction $-C_{Pb}$ and the blockage parameter β, i.e., the ratio between the projected area of the body and the cross-section area of the empty channel. For cylinders spanning across the channel, β is equal to the ratio between the diameter (the cross-stream projected dimension) and the channel width. For the simulated case under consideration (see Fig. 1) $\beta = H^{-1}$. Following Maskell [16], the blockage-corrected value of the mean separation velocity squared k_c^2 is

$$k_c^2 = a + \sqrt{a^2 - k^2}, \quad 2a = k^2 + 1 - C_D \beta. \tag{6}$$

The corrected drag coefficient (C_{D_c}) and the corrected pressure coefficients (C_{P_c}) around the body are then determined from

$$\frac{C_D}{C_{D_c}} = \frac{k^2}{k_c^2} = \frac{1 - C_P}{1 - C_{P_c}} = \alpha_q, \tag{7}$$

where $\alpha_q > 1$ is the ratio between the corrected and the actual oncoming dynamic pressure. The corrected Reynolds number is simply $\mathrm{Re}_c = \sqrt{\alpha_q} \mathrm{Re}$. It is worth noting that $C_{D_c}/C_D = \alpha_q^{-1} = 1 - C_{D_c} \beta/(-C_{Pb_c})$, where $(-C_{Pb_c})$ and C_{D_c} are constants. For unconfined flow at around the Reynolds number under consideration ($\mathrm{Re} = 2 \times 10^4$) the ratio $C_D/(-C_{Pb}) \approx 1.5$ [19–21], i.e., for low blockages and by using the Maskell scheme $\alpha_q \approx (1 - 1.5\beta)^{-1}$. Following Vickery [22], see also Bearman and Obasaju [23], Norberg [21], and Luo et al. [25], the same correction as for C_D can be applied also for the rms lift and drag coefficients, i.e.,

$$\frac{C_{L'}}{C_{L'_c}} = \frac{C_{D'}}{C_{D'_c}} = \alpha_q. \tag{8}$$

Assuming that the shedding frequency is directly proportional to the separation velocity, a corrected Strouhal number would simply be $\mathrm{St}_c = \mathrm{St}/\sqrt{\alpha_q}$. However, for the relatively low blockage ratios under consideration, $\beta \leq 10$ percent approximately, this simple procedure appears to give underestimated corrected Strouhal numbers [22,26,20]. Compared to the mean separation velocity, i.e., the mean velocity in the outer parts of the separating shear layers springing from the frontal edges, the mean velocity at around the trailing edges of the cylinder is probably more directly related to the shedding frequency [27]. At least for low blockages, it is believed that the blockage effects on the shedding frequency are significantly lower than the effective increase in the oncoming velocity. In Bearman [28], for various bluff-body shapes, it is shown that the product $C_D \times \mathrm{St}$ is roughly proportional to $(k - 1)$. Based on this finding the following new but less severe correction for the Strouhal number was applied:

$$\frac{\mathrm{St}}{\mathrm{St}_c} = \frac{k - 1}{k_c - 1} \left(\frac{C_{D_c}}{C_D} \right), \tag{9}$$

where corrected quantities on the right side are calculated from the Maskell method.

5 Results and Discussion

All calculations were carried out on one processor of a SGI ORIGIN 2000 machine. The transient period before the fully developed state is achieved was about 50 time units. The CPU time per time step and grid point was about 2.7×10^{-4}, 2.2×10^{-4}, and 1.9×10^{-4} CPU seconds for cases DSM, OEDSM, and SSM, respectively. The number of iterations per time step was about two, three, and two for cases SSM, the DSM, and the OEDSM, respectively. The reason why case OEDSM was cheaper than DSM in terms of CPU is that fewer iterations were needed at each time step, owing to better numerical stability. Global results of these three models were compared with experimental (smooth flow) ones [22,23,5,21,25,29,30] and numerical results presented at the LES workshop (LES1) [4] and in the LES2 exercise [6] (Table 2). A series of time- and spanwise-averaged resolved velocity, pressure, and turbulent stresses are also provided for comparison with

Table 2 Summary of global results including a comparison with previous LES and laboratory experiments. For LES, H and A are the lateral and spanwise dimensions of the calculation domain, respectively. For experiments (EXP), β and ℓ are the blockage parameter and the aspect ratio of the cylinder, respectively. For cases having β or H^{-1} within parenthesis the results have been adjusted due blockage effects. A bold-faced value for the aspect ratio ℓ means that the cylinder is terminated by end plates. Please note that different free stream turbulence intensities ($\leq$2 percent) are used in these experiments

LES	$\mathrm{Re}/10^3$	H^{-1} (percent)	A	St	C_D	$-C_{Pb}$	$C_{L'}$	$C_{D'}$
SSM	22	6.4	4	0.127	2.22	1.48	1.50	0.16
DSM	22	6.4	4	0.126	2.03	1.30	1.23	0.20
OEDSM	22	6.4	4	0.130	2.25	1.55	1.50	0.20
OEDSMT	22	6.4	4	0.129	2.23	1.54	1.42	0.20
OEDSMF	22	6.4	4	0.132	2.32	1.63	1.54	0.20
OEDSMF	23	(6.4)	4	0.128	2.09	1.38	1.39	0.19
OEDSMA	22	6.4	7	0.132	2.27	1.56	1.46	0.17
LES1 '95 [4]	22	7.1	4	0.07–0.15	1.7–2.8	—	0.4–1.8	0.10–0.27
LES2 '96 [6]	21.4	5.0–7.1	4	0.13–0.16	2.0–2.8	—	1.0–1.7	0.12–0.36

EXP	$\mathrm{Re}/10^3$	β (percent)	ℓ	St	C_D	$-C_{Pb}$	$C_{L'}$	$C_{D'}$
Norberg [21]	13	(1.6)	**51**	0.131	2.11	1.37	—	—
Lyn et al. [5]	21.4	7.1	9.8	0.13	$\approx$2.1	—	—	—
Norberg [21]	22	(1.6)	**51**	0.130	2.10	1.37	—	—
Bearman/Obasaju [23]	22	(5.5)	**17**	0.13	2.1	1.4	1.2	—
McLean/Gartshore [30]	23	4.2	**16**	—	—	—	1.3	—
Luo et al. [25]	34	(5.0)	**9.2**	0.13	2.21	1.52	1.21	0.18
Vickery [22]	100	(7.1)	14	0.12	2.05	1.35	1.3	0.17
Lee [29]	176	(3.6)	9.2	0.122	2.04	1.33	1.19	0.22

experiments. The time-averaged quantities were calculated over about 20 shedding cycles, except for case OEDSMT for which the time integration interval was about ten shedding cycles. The Strouhal numbers were calculated from the fluctuating lift signal. The computed resolved quantities are decomposed into a time (denoted by $\langle\rangle_t$) component and a fluctuation (denoted by $'$) component. For example, the resolved velocities are decomposed and written as $\bar{u}_i = \langle\bar{u}_i\rangle_t + u_i'$.

5.1 Comparison of Global Quantities. A summary of global results from the present simulations including a comparison with some previous experimental/simulation studies is provided in Table 2. Please note that for all simulations in Table 2 the rms lift and drag coefficients are calculated from the time-dependent, spanwise-averaged forces on the cylinder. Conversely, for all laboratory experiments in this table the rms lift and drag coefficients are sectional and measured at midspan of the cylinder. In this highly turbulent flow situation, the local fluctuating forces on the cylinder are not fully correlated along the span and thus the sectional rms forces are higher than the spanwise-averaged ones. From the present simulations the ratios between the spanwise-averaged and the spanwise-mean sectional rms forces were calculated. For rms lift the ratio was about 0.99 for all cases except for case OEDSMA, which had 0.97. The corresponding values for rms drag were 0.72, 0.80, 0.76, 0.73, 0.71, and 0.69 for cases SSM, DSM, OEDSM, OEDSMT, OEDSMF, and OEDSMA, respectively. When comparing OEDSMA with OEDSM, for which the major difference is the computational spanwise length ($A=7$ compared to $A=4$), the spanwise-averaged rms lift and drag are reduced by about 3 percent and 15 percent, respectively. However, the correct comparison should be made on sectional forces for which reductions in rms lift and drag are only about 0.7 percent and 6 percent, respectively. The reduction in $C_{D'}$ with an increase in the spanwise length is similar to that reported for Re $=200-500$ in the previous work of the present authors [9,31]. When comparing OEDSMT with OEDSM, for which the only difference is the time step ($\Delta t=0.0125$ compared to $\Delta t=0.025$), the only significant change is a 5 percent reduction in the rms lift. Again this is in accordance with previous findings of Sohankar et al. [9] (Re=500, $A=6$).

Also please note that most experimental results in Table 2 are corrected for blockage effects (these cases have original β values within parentheses). Among these, all corrections are made using the scheme of Maskell [17], as outlined in Section 4, except for Lee [29] in which the method of Allen and Vincenti [32] is used. In Lee [29] the rms lift and drag coefficients are not corrected for blockage; the $C_{L'}$ and $C_{D'}$ values provided in Table 2 have been adjusted for this effect ($\alpha_q = 1.037$).

The effects of Reynolds number can be expected to be of secondary importance for the flow case in question [20,21,23,33]. This can also be judged from the experimental results provided in Table 2. However, the blockage is a most important factor when comparing global results. For instance, when comparing the corrected results of case OEDSMF with corrected experimental results at around the same Reynolds number (Table 2) the agreement for the Strouhal number St, the mean drag coefficient C_D, and the base suction $-C_{Pb}$ is excellent. Without taking the blockage effects into account there is only a fair agreement with experiments, except perhaps for the DSM simulation which then compares rather well with the experiments. For all present simulations, the velocity increase at around the lateral boundaries for $x>0$ were in excellent agreement with the effective increase of the free stream velocity as predicted from the Maskell blockage-correction scheme ($\alpha_q \simeq 1.1$, i.e., the free stream velocity in the simulations is about 5 percent too high due to blockage). This adds to the creditability for the applied blockage corrections (Sec. 4). In comparison with experiments the rms lift and drag coefficients seem to be slightly overpredicted from the OEDSMF simulation, despite the blockage correction. Presumably, and based on the tendencies for the one-equation cases in Table 2, the combination of a larger spanwise dimension, a shorter time step, and a grid refinement would bring the levels of fluctuating forces (corrected for blockage) even closer to those indicated from the experiments ($C_{L'}\simeq1.2-1.3$, $C_{D'}\simeq0.2$). However, such a massive simulation was not feasible on the available computer. From another point of view, note that any differences in predicted results between, for example, cases OEDSM and OEDSMF will come not only from discretization errors, but also partly from the subgrid model. The reason is that the space discretization error and the contribution from the subgrid model are connected to each other, since the filter width is chosen as $\Delta=(\delta V)^{1/3}$.

Since the lateral boundaries were treated as frictionless solid walls, the present simulations are indeed susceptible to a true blockage effect. In this context, it should be noted that most (all?) simulations in the LES1 and LES2 exercises employ lateral boundary conditions which represent a freestream condition ($u=1$; $v=0$). Consequently, on global quantities, a direct comparison with these simulations is questionable and is therefore omitted. When taking into account the blockage, the DSM simulation came out worse in the comparison with experiments. The simulations using the new one-equation dynamic model (cases OEDSM, OEDSMT, OEDSMF and OEDSMA) produced similar global results, which all, when taking blockage into account, compare favorably with experiments (Table 2). The SSM simulation produced similar global results to the OEDSM, except for Strouhal
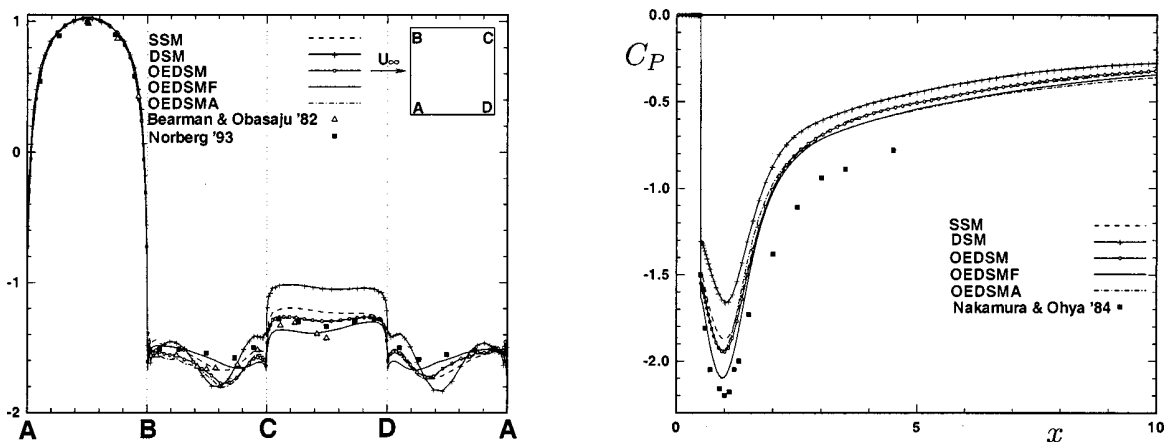

Fig. 2 Time- and spanwise-averaged pressure coefficient C_P around the cylinder (left) and versus x at centerline $y=0$ (right). Experiments: Bearman & Obasaju [23], Re=22×10³; Norberg [21], Re=13×10³; Nakamura and Ohya [38], Re=67×10³. All distributions around the cylinder (left) have been corrected for blockage using the Maskell scheme (Sec. 4)

number and rms drag, which came out slightly lower. The good agreement with experiments for all cases except DSM is further exemplified in Fig. 2 (left). In this figure all pressure distributions have been corrected for blockage effects.

The selected experimental test case for the LES1 and LES2 exercises is the LDV study of Lyn et al. [5] for which the blockage is $\beta = 7.14$ percent and the cylinder aspect ratio is $\ell = 9.75$ ($\text{Re} = 22 \times 10^3$). The measurements in Lyn et al. [5] are carried out at midspan of the cylinder and are restricted to one side of the center line ($y > 0$), apparently without any check on the assumed symmetry of this procedure. Further, it can be noted that no end plates are used in Lyn et al. [5] to shield the central flow from the tunnel wall boundary layers, which is of special importance when using such a short aspect ratio, e.g., see Cowdrey [34] and Stansby [35]. In turbulent flow the required minimum aspect ratio for obtaining global results independent of this parameter is dependent on the intrinsic degree of coherence of the near-cylinder flow along the span. In this context, the (one-sided) axial correlation length of sectional lift or lift-related quantities can be used to estimate the required (minimum) aspect ratio. The conservative guideline provided in Norberg [24] is that the aspect ratio (length-to-diameter) should be greater than about five such correlation lengths. Conceivably, with an optimized end plate design the required aspect ratio can be reduced, a reasonable estimate would be about three such correlation lengths [36]. The axial correlation length at around $\text{Re} = 22 \times 10^3$ has been reported to be within four to five diameters [23,30]. It should be emphasized that the computational spanwise length of the simulations (parameter A) should not be confused with the experimental aspect ratio (parameter ℓ) [37]. However, it should be remembered that also for three dimensional (3D) simulations the parameter A should be large enough in order to capture all dynamically significant spanwise flow features.

All experimental cases in Table 2 have a free stream turbulence intensity ≤ 0.5 percent except Lyn et al. [5] for which the upstream free stream turbulence level is reported as ≈ 2 percent. As shown, e.g., in Vickery [22], Lee [29], Nakamura and Ohya [38], and Cheng et al. [39] the effect of adding turbulence to the oncoming free stream reduces the drag, the base suction, the fluctuating lift, and the axial correlation length, respectively, effects which appear also to be dependent on the turbulence integral length scale. The present simulations did not account for any effect of free stream turbulence, as the inlet flow was prescribed as completely uniform and time independent. It is worth noting that the effects of turbulence on the flow around a square cylinder appear to be similar to an increase in the afterbody length [38]. Lyn et al. [5] report a mean drag coefficient of $C_D \approx 2.1$ (Table 2), which is about the same as the blockage-corrected mean drag coefficient of Bearman and Obasaju [23] and Norberg [21], for which the free stream turbulence intensity is less than 0.1 percent (0.04 percent and 0.06 percent). If the effect of free stream turbulence was to be negligible in Lyn et al. [5], the blockage effect alone would certainly produce a higher mean drag coefficient than is reported (the Maskell scheme predicts an increase in C_D of about 12 percent for this case). On the other hand, without taking into account the blockage, the effect of free stream turbulence would presumably give a C_D which is lower than is reported. In Lyn et al. [5] the time-averaged drag coefficient is approximated from the integral of the time-averaged streamwise momentum flux at $x = 8$. This procedure is highly questionable since the pressure field must also be accounted for [40], especially so since the flow is confined between walls. A check on the evaluation of cylinder drag from momentum principles was applied to the present simulations. The time-averaged drag calculated from a momentum balance between the inlet section (at $x = -7.9$) and sections behind the cylinder ($x > 0.5$) was within ± 0.5 percent of the time-averaged drag as calculated from the pressure and shear stresses acting on the cylinder. For all these downstream x positions, the contribution from the streamwise momentum flux was in fact

negative. As indicated above there may also in Lyn et al. [5] be significant effects due to the short aspect ratio, especially in combination with the nonoptimum end conditions. Moreover, the oncoming flow in Lyn et al. [5] is not fully described, the most upstream station being only three diameters upstream of the cylinder axis. At this upstream position ($x = -3$) the difference between the free stream velocity and the centerline velocity (at $y = 0$) is reported to be "almost 0.1" (see Lyn et al. [5], p. 289). At this position ($x = -3$, $y = 0$) the present simulations gave out a velocity difference of about 0.055.

From the above it is clear that detailed quantitative comparisons with the results of Lyn et al. [5] should be made with caution. However, the basic flow geometry in combination with the high Reynolds number are believed to be the most important factors in the flow development of the shedding wake and thus in the following section some statistical moments of resolved velocity components in the wake are presented together with corresponding experimental data of Lyn et al. [5].

5.2 Comparison of the Computed Mean Flow With Experiments. The time- and spanwise-averaged streamwise velocity $\langle \bar{u} \rangle_{tz}$ and component velocity fluctuations squared (variances) were calculated along the wake center line ($x > 0.5$, $y = 0$). In Fig. 3, $\langle \bar{u} \rangle_{tz}$ and the square root of these variances, here referred to as rms velocities ($v_{\text{RMS}} = \sqrt{\langle u'u' \rangle_{tz}}$, $v_{\text{RMS}} = \sqrt{\langle v'v' \rangle_{tz}}$, $w_{\text{RMS}} = \sqrt{\langle w'w' \rangle_{tz}}$), are shown together with the experimental results of Lyn et al. [5] at the center line of the wake. Among the simulations and for the streamwise velocity, case OEDSMF is closest to the experiments. The refinement in the $x-y$ plane (OEDSMF) and the increase of the spanwise extent (OEDSMA) have opposite effects on the predicted center line velocity. This seems to be connected to a weaker recirculation region for case OEDSMA, as the flow becomes less 2D because large spanwise flow structures are captured. For the present cases the position of zero velocity along the center line (the wake closure point) occurred at approximately one diameter downstream of the cylinder axis. This is in contrast to the experiments of Lyn et al. [5] for which the corresponding position is $x = 1.4$ (see Fig. 3). The recovery of the streamwise velocity in the intermediate wake levels off at approximately 0.87, 0.81, 0.80, 0.75, and 0.70 for cases DSM, OEDSMA, SSM, OEDSM, and OEDSMF, respectively. These values are higher than the experiment of Lyn et al. [5], which is about 0.6. Other LES calculations also report a great disparity of results in the wake region [4,6]. The reasons for this inconsistency in the simulated wake flow are unclear. However, the spatial resolution in the wake region in combination with grid stretching and the type of SGS model used seem to be important factors.

The predictions of u_{RMS} and v_{RMS} for OEDSM and OEDSMF have relatively good agreement with experiments, especially for the finer resolution (case OEDSMF) (see Fig. 3). The DSM has the lowest rms velocities, with larger discrepancies with experiments. It can be noted that there was a correspondence between the rms levels of near-wake velocity fluctuations and forces on the cylinder (see Table 2). There seem not to be any spanwise rms velocities w_{RMS} in the literature for a direct comparison with the present results.

A connection between the velocity level in the wake and drag and pressure coefficients was noted. Case DSM, with a higher center line velocity level off, predicts lower drag force, whereas the opposite trend is observed in OEDSM. As is seen in Fig. 2 (right), the OEDSMF gives higher negative pressure at the center line while the DSM has lower values. The maximum (negative) pressure is located at around $x = 1$, with values of -2.10 and -1.66 for the OEDSMF and DSM, respectively. Such a difference is also observed in the pressure around the body, see Fig. 2 (left). In Fig. 2 (right) the experimental results of Nakamura and Ohya [37] for the static pressure variation along the wake center line at $\text{Re} = 67 \times 10^3$ ($\beta = 2.5$ percent, aspect ratio $\ell = 17$, free stream turbulence intensity 0.12 percent) have been included for
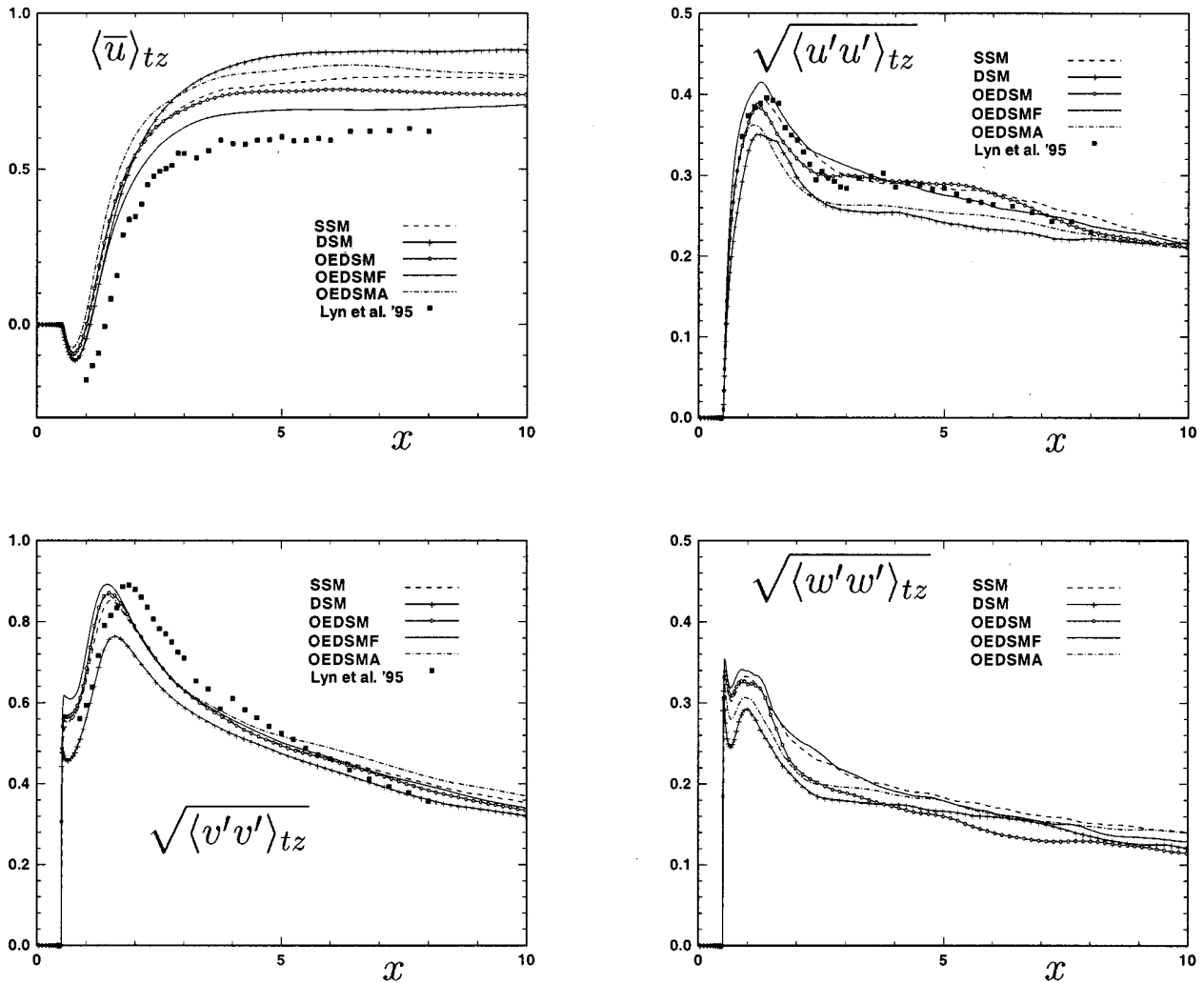
Fig. 3 Time- and spanwise-averaged velocity $\langle \bar{u} \rangle_{tz}$, and RMS velocities ($\sqrt{\langle u'u' \rangle_{tz}}$, $\sqrt{\langle v'v' \rangle_{tz}}$, $\sqrt{\langle w'w' \rangle_{tz}}$) at center-line ($y=0$)

comparison with present results, which in this figure are given without any blockage corrections. Since the mean static pressure within a highly turbulent flow cannot be measured with ''any assurance of accuracy in laboratory flows'' [41] the comparison with present simulations can only be made qualitatively. Nevertheless, the position of minimum pressure is believed to be accurately captured in these experiments and concerning this position there is a good agreement with the present simulations. Figure 2 (left) shows time-and spanwise-averaged pressure coefficients around the body, together with the experimental results of Norberg [21] for Re=13×10^3 and Bearman and Obasaju [23] for Re =22×10^3. All results in this figure have been corrected for blockage effects using the Maskell scheme (Sec. 4). As is seen in this figure, all cases except for case DSM compare favorably with the experiments.

The time- and spanwise-averaged streamwise velocities versus y together with experimental results [5] at two different streamwise positions ($x=2.5,6.5$) are shown in Fig. 4. The best agreement between the present results and experimental ones is for the OEDSMF. As in most of the cases, the difference between the SSM and the OEDSM results is relatively small. Of these cases, again the DSM shows the largest discrepancies with experiments.

Figure 5 shows the time- and spanwise-averaged normal and shear Reynolds stresses versus y together with experimental re-

sults of Lyn et al. [5] at two different streamwise positions (x =2.5,6.5). In general, small resolved shear stresses reduce the exchange of momentum in the y direction, giving a less ''full'' velocity profile. This can also be seen in Figs. 4 and 5, where OEDSMF gives a less ''full'' velocity profile than the other cases, and that OEDSMF gives the lowest resolved shear stresses.

Figure 4 shows the time- and spanwise-averaged normalized turbulent eddy viscosity ($\nu_r = \nu_t / \nu$) versus y at two different streamwise positions ($x=2.5,6.5$). In the wake flow, the lowest value of ν_t (or ν_r) is predicted with the SSM and the highest values with the DSM at $x=2.5$. At $x=6.5$, all cases except SSM are relatively similar. In the wake flow, the maximum level of the eddy viscosity for the DSM is approximately two and four times greater than the values for OEDSM and SSM, respectively. Overall, the lowest and the highest values of the eddy viscosities are predicted by the SSM and the DSM, respectively. Large subgrid viscosity generally increases the dissipation of the resolved flow, and consequently dampens the resolved fluctuations. This can be seen in Figs. 4 and 5, where high subgrid viscosity corresponds to small resolved normal Reynolds stresses (case DSM) or vice versa (case SSM).

By studying all components of the normal Reynolds stresses in the computational domain for different cases, it is observed that the DSM predicts the lowest level for all components of the Rey-
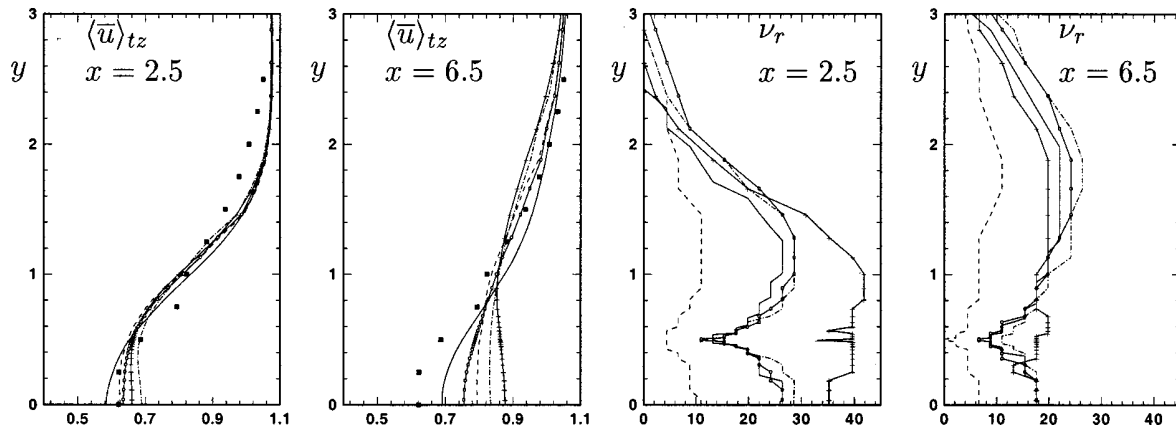
Fig. 4 Time- and spanwise-averaged velocity $\langle \bar{u} \rangle_{tz}$ and ratio of turbulent viscosity $\nu_r = \nu_t / \nu$ versus y at $x = 2.5$ and $x = 6.5$ (see Fig. 2 for legend)
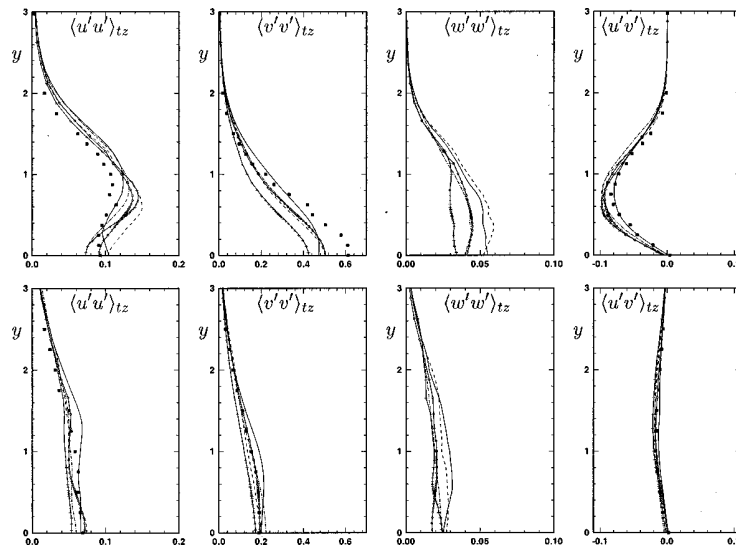

Fig. 5 Time- and spanwise-averaged turbulent stresses ($\langle u'u' \rangle_{tz}, \langle v'v' \rangle_{tz}, \langle w'w' \rangle_{tz}, \langle u'v' \rangle_{tz}$) versus y at $x = 2.5$ (top) and $x = 6.5$ (bottom) (see Fig. 2 for legend)

nolds stresses. The DSM also predicts higher base and minimum pressure coefficients at the center line of the wake as compared with the other cases. It is possible to conclude that the lower Reynolds stresses correspond to a higher pressure region in the wake flow. A higher base pressure gives a lower drag force. Thus, the lower predicted Reynolds stresses for the DSM lead to a higher pressure region in the wake, which causes lower drag force (see Table 2). Similar results are also reported by Mittal and Balachandar [42] for circular and elliptic cylinders (Re=525).

5.3 Results for the One-Equation Subgrid Model. Three subgrid-scale models were used in this study. Of these three models, the one-equation subgrid model was successful in accounting for the backscattering phenomenon of the inverse energy transfer from the subgrid scales to the resolved scales [43]. In this section, this phenomenon is examined by studying the SGS production, $P_{k_{sgs}}$, in the k_{sgs} equation [see Eqs. (1) and (2)]. When the dynamic coefficient C^k [see Eq. (3)] becomes negative, the production $P_{k_{sgs}}$, becomes negative. This is in this study defined as backscatter.

Figure 6 (left) shows the time history of the local dynamic coefficient C^k at two chosen points at midspan and center line of the body ($z = 0$, $y = 0$) for case OEDSMA. At the point located close to the downstream face of the body ($x = +0.7$), the range of variation of C^k is most of the time ± 0.5. The range of variation of C^k with time is much smaller in the stagnation region upstream of the body than in shear layers and the wake region. A similar variation of C^k with time was also observed for cases OEDSM and OEDSMF [44]. Interestingly, C^k has a negative value for all times and all spanwise locations in the stagnation region in front of the body. This is seen for $x = -0.7$ in Fig. 6 (left), for which the time-averaged value is equal to -0.07. The negative values of C^k, or negative eddy viscosity, cause the SGS production term in the turbulent kinetic subgrid energy to become negative [see Eq. (2)]. Such negative SGS production in the stagnation region in front of the body is also seen for case OEDSMA in Fig. 7 (left). There are also negative instantaneous C^k values with time in other regions, e.g., in the free shear layers and in the wake. Thus, the sign of the time-averaged SGS production term depends on
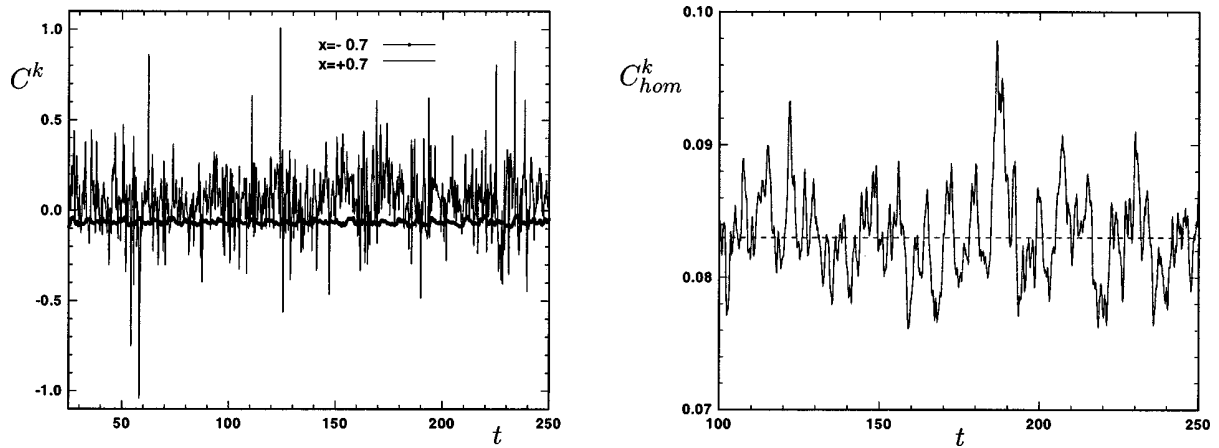
Fig. 6 Time variation of C^k at two chosen cells on the centerline $y=0$ (left) and C^k_{hom} (right) for case OEDSMA
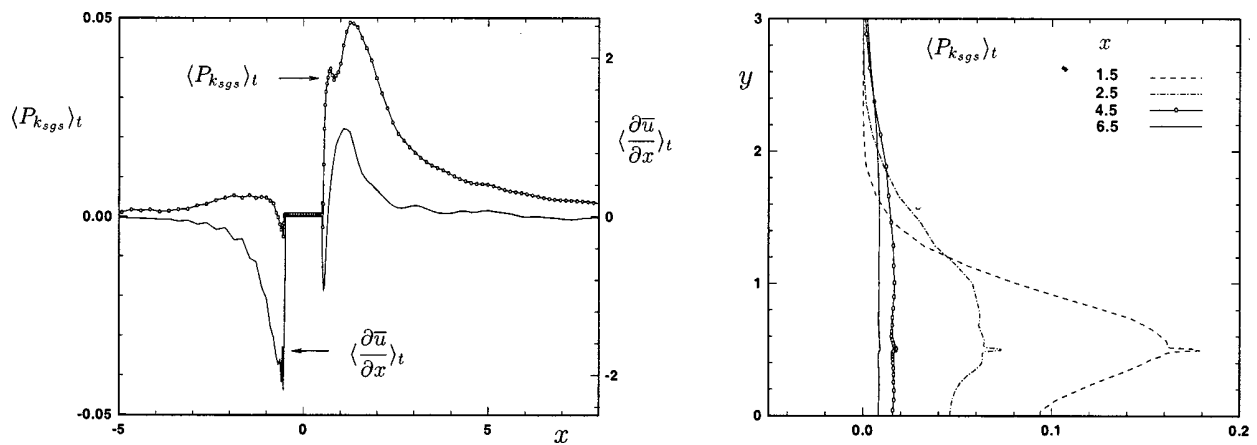

Fig. 7 Time-averaged SGS production ($\langle P_{k_{sgs}} \rangle_t$) and velocity gradient ($\langle \partial \bar{u}/\partial x \rangle_t$) at midspan ($z=0$) for case OEDSMA. Along centerline $y=0$ (left); at different streamwise locations versus y (right).

whether there is negative production (backscatter) or positive production (forward scatter). In the wake region, the time-averaged SGS production is positive and decreases in the streamwise direction, see Fig. 7 (right). The two peaks that appear in the SGS production in Fig. 7 (right) at $y \simeq 0.5$ (corresponding to the top of the cylinder) are due to the refinement of the grid in this region. As the grid in the y direction in this region is very fine, it means that a large part of the turbulence is locally resolved, which gives rise to large velocity gradient and thus a large $P_{k_{sgs}}$.

As noted earlier, the local dynamic coefficient C for the dynamic model has a large variation in space and time [44]. This large oscillation in C enters directly into the momentum equations via eddy viscosity, which can enhance numerical instability problems. It is also observed that the dynamic model produces more wiggles upstream of the body than do other models [44]. These extra wiggles are produced as a result of numerical problems associated with the negative values and a large variation in the dynamic coefficient. In the OEDSM, the local dynamic coefficient C^k enters into the source terms of the turbulent kinetic subgrid energy equation. To ensure numerical stability, a *homogeneous* value of C^k in space (C^k_{hom}) is used in the momentum equations, which is determined by Eq. (5). This procedure increases the numerical stability by preventing large oscillations in the subgrid viscosity in the momentum equations. The time history of C^k_{hom} is shown in Fig. 6 (right). The range of variation of C^k_{hom} with time

is between about 0.075 and 0.10 with a time-averaged value of 0.083 for case OEDSMA (dashed line). The time-averaged value of C^k_{hom} is 0.085 for the case OEDSM. This time-averaged value is different for different flow configurations. For example, the value for recirculating flow is reported to be 0.04 [15]. For transitional flow behind a backward-facing step, a value of 0.07 is found [45]. Due to the relatively small variation of the homogeneous time-dependent dynamic coefficient, no sign of numerical problems was observed. It should be mentioned that the dynamic one-equation model has also been applied successfully to plane channel flow and to the flow around a surface-mounted cube [46].

6 Conclusions

LES of the flow around a square cylinder at $Re=22\times10^3$ and for a solid blockage of $\beta=6.4$ percent is presented. Three different subgrid scale models: the Smagorinsky, the standard dynamic, and a dynamic one-equation model, are applied. Among these three models, the lowest level of all components in the Reynolds stress tensor is predicted by the dynamic model. This model also predicts higher pressure in the wake region. It is concluded that the lower Reynolds stresses correspond to a higher pressure region in the wake flow, which leads to lower drag forces.

In spite of the fact that the CPU time for each iteration in the case of the one-equation model is higher than for the dynamic model, the CPU time required at each time step is higher for the

dynamic model. This is a consequence of numerical problems associated with the dynamic model that increase the number of iterations for convergence at each time step.

By comparison with experiments, the results produced by the dynamic one-equation model give better agreement with experiments than the other two subgrid models. Another important advantage of the dynamic one-equation model is that it does not involve any free constants as the Smagorinsky model does. Furthermore, contrary to the standard dynamic model, the dynamic one-equation model does not require any arbitrary clipping or averaging of dynamic coefficients to achieve numerical stability. Due to the relatively small variation in the homogeneous time-dependent dynamic coefficient in this model, no sign of numerical problems, which are seen for standard dynamic model, is observed.

Influences of spatial and temporal resolution and the computational spanwise length, respectively, are only presented for simulations using the one-equation subgrid model. Using a finer spatial resolution in the cross-sectional plane improves the agreement between predictions and experiments and when also taking into account blockage effects there is a very good agreement. In fact, the effects of blockage are shown to be very important for the case under consideration, and for a correct comparison with experiments these effects have to be accounted for. By increasing the spanwise dimension from four to seven diameters (side lengths) there is a 6 percent reduction in sectional rms drag, while other global quantities are within ± 2 percent. By increasing the time resolution by a factor of 2 the only significant change is a 5 percent reduction in the rms lift.

References

[1] Sakamoto, S., Murakami, S., and Mochida, A., 1993, ''Numerical Study on Flow Past 2D Square Cylinder by Large Eddy Simulation,'' J. Wind Eng. Ind. Aerodyn., **50**, pp. 61–68.

[2] Yang, K.-S., and Ferziger, J., 1993, ''Large-Eddy Simulation of Turbulent Obstacle Flow Using a Dynamic Subgrid-Scale Model,'' AIAA J., **31**, pp. 1406–1413.

[3] Murakami, S., and Mochida, A., 1995, ''On Turbulent Vortex Shedding Flow Past 2D Square Cylinder Predicted by CFD,'' J. Wind Eng. Ind. Aerodyn., **54**, p. 191.

[4] Rodi, W., Ferziger, J., Breuer, M., and Pourquié, M., 1997, ''Status of Large-Eddy Simulations: Results of a Workshop,'' ASME J. Fluids Eng., **119**, pp. 248–262.

[5] Lyn, D. A., Einav, S., Rodi, W., and Park, J. H., 1995, ''A Laser-Doppler Velocimetry Study of the Ensemble-Averaged Characteristics of the Turbulent Near Wake of a Square Cylinder,'' J. Fluid Mech., **304**, pp. 285–319.

[6] Voke, P. R., 1997, ''Flow Past a Square Cylinder: Test Case LES2,'' *Direct and Large Eddy Simulation II*, J. P. C. Challet, P. Voke, L. Kouser, eds., Kluwer Academic, Dordrecht.

[7] Rodi, W., 1997, ''Comparison of LES and RANS Calculations of the Flow Around Bluff Bodies,'' J. Wind Eng. Ind. Aerodyn., **69–71**, pp. 55–75.

[8] Williamson, C. H. K., 1996, ''Vortex Dynamics in the Cylinder Wake,'' Annu. Rev. Fluid Mech., **28**, pp. 477–539.

[9] Sohankar, A., Norberg, C., and Davidson, L., 1999, ''Simulation of Unsteady Three-Dimensional Flow Around a Square Cylinder at Moderate Reynolds Numbers,'' Phys. Fluids, **11**, No. 2, pp. 288–306.

[10] Smagorinsky, J., 1963, ''General Circulation Experiments with the Primitive Equations,'' Mon. Weather Rev., **91**, pp. 99–165.

[11] Moin, P., and Kim, J., 1982, ''Numerical Investigation of Turbulent Channel Flow,'' J. Fluid Mech., **118**, pp. 341–377.

[12] Germano, M., Piomelli, U., Moin, P., and Cabot, W., 1991, ''A Dynamic Subgrid-Scale Eddy Viscosity Model,'' Phys. Fluids A, **3**, pp. 1760–1765.

[13] Lilly, D., 1992, ''A Proposed Modification of the Germano Subgrid-Scale Closure Method,'' Phys. Fluids A, **4**, pp. 633–635.

[14] Akselvoll, K., and Moin, P., 1995, Large eddy simulation of turbulent confined coannular jets and turbulent flow over a backward facing step. Report No. TF-63, Department of Mechanical Engineering Stanford University.

[15] Davidson, L., 1997, ''Large Eddy Simulation: A Dynamic One-Equation Subgrid Model for Three-Dimensional Recirculating Flow,'' *11th International Symposium on Turbulent Shear Flow*, Grenoble, Vol. 3, pp. 26.1–26.6.

[16] Ghosal, S., Lund, T., Moin, P., and Akselvoll, K., 1995, ''A Dynamic Localization Model for Large-Eddy Simulation of Turbulent Flows,'' J. Fluid Mech., **286**, pp. 229–255.

[17] Maskell, E. C., 1963, ''A Theory of the Blockage Effects on Bluff Bodies and Stalled Wings in a Closed Wind Tunnel,'' Reports and Memoranda 3400, Aeronautical Research Council (ARC).

[18] Modi, V. J., and El-Sherbiny, S. E., 1971, ''Effect of Wall Confinement on Aerodynamics of Stationary Circular Cylinders,'' *3rd International Conference on Wind Effects on Buildings and Structures*, Saikon Shuppan Co., Ltd., Tokyo, Volume 2, pp. 365–376.

[19] Okajima, A., and Sugitani, K., 1984, ''Strouhal Number and Base Pressure Coefficient of a Rectangular Cylinder,'' Trans. Jpn. Soc. Mech. Eng., Ser. B, **50**, pp. 2004–2012.

[20] Igarashi, T., 1984, ''Characteristics of the Flow Around a Square Prism,'' Bull. JSME, **27**, pp. 1858–1865.

[21] Norberg, C., 1993, ''Flow Around Rectangular Cylinders: Pressure Forces and Wake Frequencies,'' J. Wind Eng. Ind. Aerodyn., **19**, pp. 187–196.

[22] Vickery, B. J., 1966, ''Fluctuating Lift and Drag on a Long Cylinder of Square Cross-Section in a Turbulent Stream,'' J. Fluid Mech., **25**, pp. 481–494.

[23] Bearman, P. W., and Obasaju, E. D., 1982, ''An Experimental Study of Pressure Fluctuations on Fixed and Oscillating Square-Section Cylinders,'' J. Fluid Mech., **119**, pp. 297–321.

[24] Norberg, C., 1994, ''An Experimental Investigation of the Flow Around a Circular Cylinder: Influence of Aspect Ratio,'' J. Fluid Mech., **258**, pp. 287–316.

[25] Luo, S. C., Yazdani, M. G., Chew, Y. T., and Lee, T. S., 1994, ''Effects of Incidence and Afterbody Shape on Flow Past Bluff Cylinders,'' J. Wind Eng. Ind. Aerodyn., **53**, pp. 375–399.

[26] West, G. S., and Apelt, C. J., 1982, ''The Effects of Tunnel Blockage and Aspect Ratio on the Mean Flow Past a Circular Cylinder with Reynolds Numbers Between 10^4 and 10^5,'' J. Fluid Mech., **114**, pp. 361–377.

[27] Igarashi, T., 1985, ''Characteristics of the Flow Around Rectangular Cylinders (The Case of the Angle of Attack 0 deg.),'' Bull. JSME, **28**, pp. 1690–1696.

[28] Bearman, P. W., 1967, ''On Vortex Street Wakes,'' J. Fluid Mech., **28**, No. 4, pp. 625–641.

[29] Lee, B. E., 1975, ''Some Effects of Turbulence Scale on the Mean Forces on a Bluff Body,'' J. Ind. Aerodyn., **1**, pp. 361–370.

[30] McLean, I., and Gartshore, C., 1992, ''Spanwise Correlations of Pressure on a Rigid Square Section Cylinder,'' J. Wind Eng. Ind. Aerodyn., **41–44**, pp. 779–808.

[31] Sohankar, A., Norberg, C., and Davidson, L., 1999, Numerical Simulation of Flow Past a Square Cylinder, *FEDSM99-7172—3rd ASME/JSME Joint Fluids Engineering Conference*, San Francisco, CA, July 18-23, American Society of Mechanical Engineers (ASME), pp. 1–6.

[32] Allen, H. J., and Vincenti, W. G., 1944, Wall interference in a two-dimensional-flow wind tunnel, with consideration of the effect of compressibility, NACA Report No. 982, National Advisory Committee for Aeronautics, Washington, D.C.

[33] Okajima, A., 1982, ''Strouhal Numbers of Rectangular Cylinders,'' J. Fluid Mech., **123**, pp. 379–398.

[34] Cowdrey, C. F., 1963, A note on the use of end plates to prevent three-dimensional flow at the ends of bluff cylinders, Current Papers ARC C.P. 683, Aeronautical Research Council (ARC).

[35] Stansby, P. K., 1974, ''The Effects of End Plates on the Base Pressure Coefficient of a Circular Cylinder,'' Aeron J., **78**, pp. 36–37.

[36] Szepessy, S., and Bearman, P. W., 1992, ''Aspect Ratio and End Plate Effects on Vortex Shedding From a Circular Cylinder,'' J. Fluid Mech., **234**, pp. 191–217.

[37] Henderson, R. D., 1997, ''Nonlinear Dynamics and Pattern Formation in Turbulent Wake Transition,'' J. Fluid Mech., **352**, pp. 65–112.

[38] Nakamura, Y., and Ohya, Y., 1984, ''The Effects of Turbulence on the Mean Flow Past Two-Dimensional Rectangular Cylinders,'' J. Fluid Mech., **149**, pp. 255–273.

[39] Cheng, C. M., Lu, P. C., and Chen, R. H., 1992, ''Wind Loads on Square Cylinder in Homogenous Turbulent Flows,'' J. Wind Eng. Ind. Aerodyn., **41–44**, pp. 739–749.

[40] Schlichting, H., 1979, *Boundary-Layer Theory*, 7th ed., McGraw-Hill, New York.

[41] Bradshaw, P., 1971, *An Introduction to Turbulence and its Measurement*, Pergamon, New York.

[42] Mittal, R., and Balachandar, S., 1995, ''Effect of the Three-Dimensionality on Lift and Drag of Nominally Two-Dimensional Cylinders,'' Phys. Fluids, **7**, pp. 1841–1865.

[43] Domaradzki, J. A., 1997, ''Backscatter Models for Large Eddy Simulations,'' Theor. Comput. Fluid Dyn., **9**, pp. 75–83.

[44] Sohankar, A., 1998, Numerical Study of Laminar, Transitional and Turbulent Flow Past Rectangular Cylinders. Ph.D. thesis, Department of Thermo and Fluid Dynamics, Chalmers University of Technology, Gothenburg.

[45] Davidson, L., and Nielsen, P., 1998, in ''A Study of Low-Reynolds Number Effects in Backward-Facing Step Flow Using Large Eddy Simulations,'' *6th International Conference on Air Distributions in Rooms, ROOMVENT'98*, E. Mundt and T. Malmström, eds., Stockhom, Sweden, Vol. 1, pp. 125–132.

[46] Krajnović, S., and Davidson, L., 1999, ''Large-Eddy Simulation of the Flow Around a Surface Mounted Cube using a Dynamic One-Equation Subgrid Model,'' *The First International Symposium on Turbulence and Shear Flow Phenomena*, S. Baneyee and J. K. Eaton, eds., Santa Barbara, Sept. 12–15.